

Bayesian estimation of 2-D P -velocity models from active seismic arrival time data: imaging of the shallow structure of Mt Vesuvius (Southern Italy)

A. Zollo,¹ L. D’Auria,¹ R. De Matteis,² A. Herrero,^{1,4} J. Virieux³ and P. Gasparini¹

¹Dipartimento di Scienze Fisiche, Università di Napoli ‘Federico II’

²Dipartimento di Studi Geologici e Ambientali, Università del Sannio, Benevento

³Géoscience Azur, UNSA-CNRS, Valbonne, Nice

⁴Istituto Nazionale di Geofisica, Roma

Accepted 2002 June 8. Received 2002 March 1; in original form 2001 March 16

SUMMARY

A multi-2-D non linear traveltimes tomography of the shallow (3–4 km deep) structure of Mt Vesuvius volcano was performed. Data have been collected during two recent active seismic experiments using a total of 17 on-land shots and about 140 three-component digital seismographs. A newly developed technique for imaging the volcano velocity structure has been applied, based on an adaptive model space investigation where the number of grid nodes is progressively increased (multi-scale approach). The optimal model parametrization is chosen according to the minimum of the Akaike Information Criteria (AIC) parameter. This corresponds to finding the best compromise between the data misfit and simplicity of the model. The model parameter estimate is performed through the computation of an *a posteriori* probability density function (pdf), defined following the Bayesian approach. The maximum likelihood model is searched by an optimization technique which combines the genetic and simplex algorithms. The evaluation of the *a posteriori* pdf is based on traveltimes computations using ray tracing techniques. Constraints on the model parameters are inserted in the form of prior pdf and error maps are inferred from cross-sections of the posterior probability around the found best fit solution. The retrieved images of Mt Vesuvius volcano show variable P -velocities in the range 1700–5800 m s⁻¹. A fairly detailed image of the top of the Mesozoic carbonate rocks forming the basement of the volcanic area is obtained. A 9 km long, 1 km deep depression was detected at the N side of the volcano. The presence of a shallow high velocity body is evidenced underneath the Mt Somma caldera and it can be interpreted as a sub- or palaeovolcanic structure.

Key words: Bayesian estimation, Mt Vesuvius, seismic tomography.

1 INTRODUCTION

High resolution seismic imaging of complex geological structures is a difficult task due to the sparse coverage of the target volume by observations, the presence of strong lateral heterogeneity of the velocity field and the irregular morphology of earth topography. However, a well refined knowledge of the 2-D/3-D background velocity model is required for research or industrial purposes, to construct reliable subsurface geological models and to accurately migrate at depth reflected/converted arrivals.

In the recent years, traveltimes tomography has become an useful tool to investigate the smooth velocity variations in complex geological environments and it is also applied to industrial purposes. It has been successfully applied to computing static corrections used for the imaging of overthrust structures (Zhu *et al.* 1992, 1998).

The inner structure of a strato-volcano, as the Somma–Vesuvius complex, is expected to show highly heterogeneous P -velocity properties. This is due to the variety of rocks forming the volcano complex (massive lavas, vesiculated lavas, consolidated tuffs, other unconsolidated pyroclastic rocks and non-volcanic rocks), the presence of dense fracture systems possibly percolated by gas and/or fluids, the presence of near-conduits, fragile rock volumes weakened by repeated magma ascent episodes and by caldera collapses and the possible occurrence of melt or partially molten bodies at shallow/intermediate depths underneath the volcano.

First- P arrival time tomography has been applied worldwide to retrieve images of shallow and deep volcano structures. In most cases the sources used were local earthquakes, i.e. at Kilauea volcano in Hawaii, (Thurber 1984), Campi Flegrei in Italy, (Aster & Meyer 1988), Mt St Helens in the USA, (Lees & Crosson 1989),

Redoubt volcano in Alaska, (Benz & Smith 1984), NE Japan volcanoes (Zhao *et al.* 1992) and Mt Etna (De Luca *et al.* 1997). High resolution active seismic experiments were also successfully applied to investigate Mt Dore volcano in France (Nercessian *et al.* 1984), Medicine Lake in California, (Evans & Zucca 1988), Jasper seamount in California, (Hammer *et al.* 1994), Mt Vesuvius in Southern Italy, (Zollo *et al.* 1998) and Reunion Island (Gallart *et al.* 1999). The input data sets for such studies are body wave arrival times from active source (on land borehole explosions and offshore airgun shots) and/or microearthquake seismic recordings acquired in various 2-D and 3-D source and receiver geometries. The use of active sources in local seismic tomography studies are revealed to be very efficient as they minimize the usual complications with local earthquake tomography which originate from the natural trade-off among the unknown source (especially the depth) and medium parameters.

In the present study, we have applied a Bayesian approach to image by seismic tomography, the shallow structure of Mt Vesuvius volcano and the surrounding plain. The problem of velocity field estimation is solved through the computation, during the model space exploration, of the *a posteriori* probability density function (pdf) which relates the observed to predicted arrival time data. This approach provides a maximum likelihood velocity model and is revealed to be particularly useful for mapping errors on parameters and for selecting the optimal medium parametrization (number of grid nodes). The latter is obtained by applying the Akaike Information Criterion (Akaike 1974) which integrates the concepts of best misfit and simplicity of the model (small number of parameters).

The search for the maximum likelihood model in the multi-dimensional parameter space is performed by a non linear optimization method which combines the Genetic (Goldberg 1989; Whitley 1994) and Simplex (Press *et al.* 1986) algorithms. Based on a discretized form of the 2-D target medium, the strategy for model space exploration consists of progressive steps. At each step the number of grid nodes is increased. This is roughly equivalent to moving from a low to high wavenumber description of the velocity field. A similar inversion strategy (called the 'multi-scale' approach) was first introduced in seismic exploration by Bunks *et al.* (1995) who applied it to seismic waveform inversion. More recently, Jin & Beydoun (2000) combined a local with global non linear optimization methods to estimate the 2-D background velocity field at different scales by analyzing image gathers after iterative pre-stack depth migrations.

The method presented in this work has been applied to data collected during the 1994 and 1996 active seismic campaigns performed in the Mt Vesuvius volcanic area which are described by Gasparini & TomoVes Working Group (1998).

2 VOLCANOLOGICAL AND GEOPHYSICAL SETTING

Mt Vesuvius belongs to the Neapolitan volcanic region, which also includes the Campi Flegrei and Ischia volcanic complexes. This region is located on the coastal Campanian Plain, which has undergone significant subsidence during the Pleistocene (Ippolito *et al.* 1973). The volcanic activity in this region began during the Pleistocene, as shown by palaeontologic and radiometric dating.

The main information on the shallow structure of Mt Vesuvius comes from a deep borehole drilled by AGIP (Italian Petroleum Agency) at Trecase on its SE slope (see Fig. 1). The well reached

the Mesozoic carbonatic rocks at a depth of 1700 m b.s.l. (Principe *et al.* 1987). The overlaying volcano-sedimentary sequence has a thickness of about 1500 m and is composed mainly of subaerial and submarine lavas alternated with pyroclastic rocks and shallow-water sediments. The chemical composition of volcanic rocks range from phonolite to tephrite. The dating of the oldest volcanic rocks in this sequence gives an approximate age of 300 kyr (Principe *et al.* 1987).

This volcano-sedimentary sequence ends with the Campanian Ignimbrite formation, a huge pyroclastic flow deposit, with a thickness of about 100 m, emplaced during a major ignimbritic eruption dated at 35–39 kyr. The vents of this eruption are probably located in Campi Flegrei or in the Campanian Plain, some kilometres north of the city of Naples (Scandone *et al.* 1991).

The shallower rocks are the pre-caldera Somma lavas that constitute the Somma volcanic edifice, with an age of about 27 ky and the pyroclastic rocks of Plinian and sub-Plinian Somma–Vesuvius eruptions with ages ranging from 20 ky to present. The mean composition of Somma lavas is between latite and phonolitic tephrite, while the pyroclastic deposit emplaced during explosive eruption (with fall, flow and surge mechanism) ranges from trachyte to tephritic phonolite.

During the last 20 ky seven Plinian eruptions have occurred at Somma–Vesuvius with a mean interval of occurrence of several thousand years. Following the famous Pompeii eruption of 79 A.D., were three further sub-Plinian eruptions in 472, 512 and 1631 A.D. From 1638 to 1944 Mt Vesuvius underwent almost continuous strombolian activity with occasional moderately explosive eruptions (e.g. 1822, 1906, 1944). Since the 1944 eruption, Mt Vesuvius entered in a quiescent stage characterized by small fumarolic activity and moderate microearthquake activity (about 100 events per year) with the maximum magnitude event ($M_D = 3.6$) recorded on October 1999.

In the early 1970's, a seismic reflection survey at sea, carried out by Osservatorio Geofisico Sperimentale in the Bay of Naples, identified a WNW-deepening strong reflector that was interpreted as the top of the Mesozoic rocks (Finetti & Morelli 1974). The depth and shape of this interface beneath Mt Vesuvius has been inferred by Bouguer anomalies calibrated with the offshore seismic reflection data and the Trecase borehole data. Bruno *et al.* (1998) have recently mapped the reflector depth around Mt Vesuvius using migrated reflection data by AGIP. A large positive magnetic anomaly centred on the volcano is observed from a regional aeromagnetic survey (Cassano & La Torre 1987), is attributed to the high magnetic susceptibility of volcanic rocks.

A large spatial variability of *P*-wave velocities (between 1.5 km s⁻¹ and 5 km s⁻¹) in the overlaying volcano-sedimentary layer is observed from 1-D traveltimes analyses using the $\tau - p$ method (De Matteis *et al.* 1997, 2000). These are consistent with laboratory measurement on rock samples from the Trecase well (Bernard & Zamora 2000).

A preliminary 2-D image of the Mt Vesuvius structure obtained by the joint linearized inversion of active earthquake and seismic data along one single profile was presented and discussed by Zollo *et al.* (1998).

3 DATA ACQUISITION AND PREPARATION

The acquisition lay-out of the active seismic experiments performed in the Mt Vesuvius area during 1994 and 1996 is illustrated in Fig. 1. Seismic sources were provided by 17 shots produced by 250 to

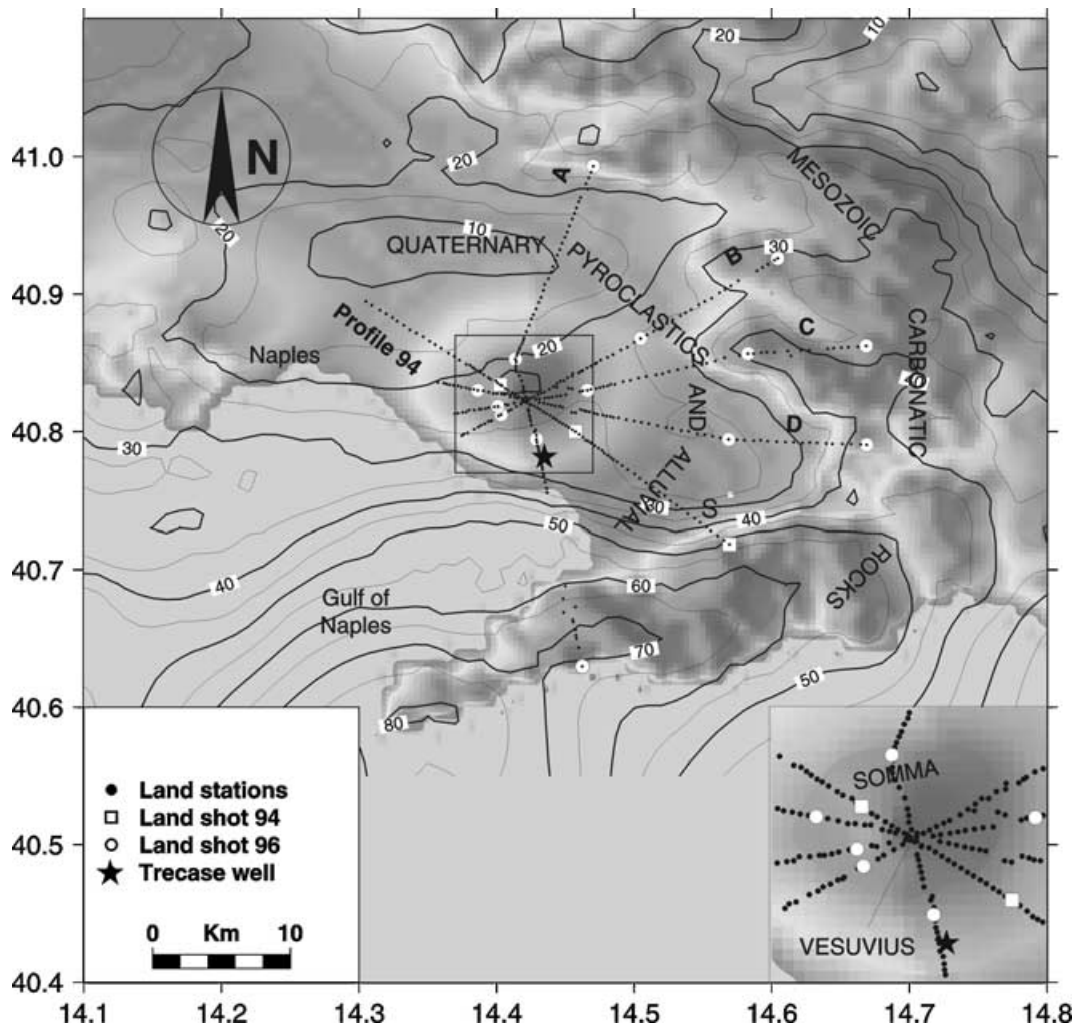


Figure 1. Map of the investigated area with the acquisition lay-out. Numbers on axes represent latitude and longitude in degrees. Bouguer anomalies are also shown (contour interval: 5 mgal). The inset represents a zoom on the crater area. The gray shading indicates the topography.

800 kg of seismic gel housed in 50 m deep boreholes. Shots and receivers were deployed along five 25 to 40 km long profiles (A, B, C, D, S in Fig. 1).

Profile S was performed in 1994 using 80 three-component seismographs which recorded three shots. Profiles A, B, C and D were carried out in 1996. During this campaign, 140 digital seismographs were deployed in the field. Each of them was equipped with three-component sensors having a natural frequency ranging between 2 and 4 Hz. The acquisition lay-out was planned according to a multi-2-D source and receiver configuration (Fig. 1.) The high population density and urban noise of the area severely affected the choice of shots and source sites. Sources and receivers were deployed along two pairs of quasi orthogonal profiles (A–C and B–D in Fig. 1). Seismic signals of each shot were recorded simultaneously along the longitudinal and the quasi-orthogonal directions (e.g. shot A1 was recorded simultaneously along the profiles A and C).

The station spacing was about 250 m on the volcano edifice and about 500 m outside. GPS and levelling measurements provided station and source coordinates with an uncertainty <10 m in vertical and <5 m in the horizontal coordinates. The sampling rate on the seismic records is 200 samples per sec. Examples of recorded sections along profiles A and C for shots located at the edge of the profiles are shown in Fig. 2. Clear first arrivals are detected from as

far as 25 km. Hand-picking of first arrival times have been performed on unfiltered and filtered seismic sections.

A non-conventional picking procedure has been applied in order to gain additional information on the medium velocities from less quality seismic recordings. On a given seismogram, generally two time pickings t_A , t_B are possible. t_A marks the first P -arrival time reading while t_B (greater than t_A) is the maximum time limit for the expected first arrival. The window $t_B - t_A$ expresses the uncertainty on the first arrival picking and accounts for possible phase misidentification, i.e. t_B could mark the arrival of an alternative P phase (e.g. reflected). Typical $t_B - t_A$ values range from 0.02 s to 0.2 s for Mt Vesuvius data. As detailed below, the value $t_B - t_A$ is used for data weighting during the optimization procedure by assigning smaller weights to data for which large windows have been measured.

It is difficult to recognize the first- P arrival, especially at large offsets, due to the relatively low signal to noise amplitude ratio, while secondary late reflected/converted arrivals can show dominant amplitudes on seismograms. In these cases, only the arrival time of the early prominent secondary arrival (t_C) observed on the seismogram can be picked. We used this time to set the *a priori* constraints on the velocity model parameters as described in the next section. In the optimization procedure, the time t_C is not used for

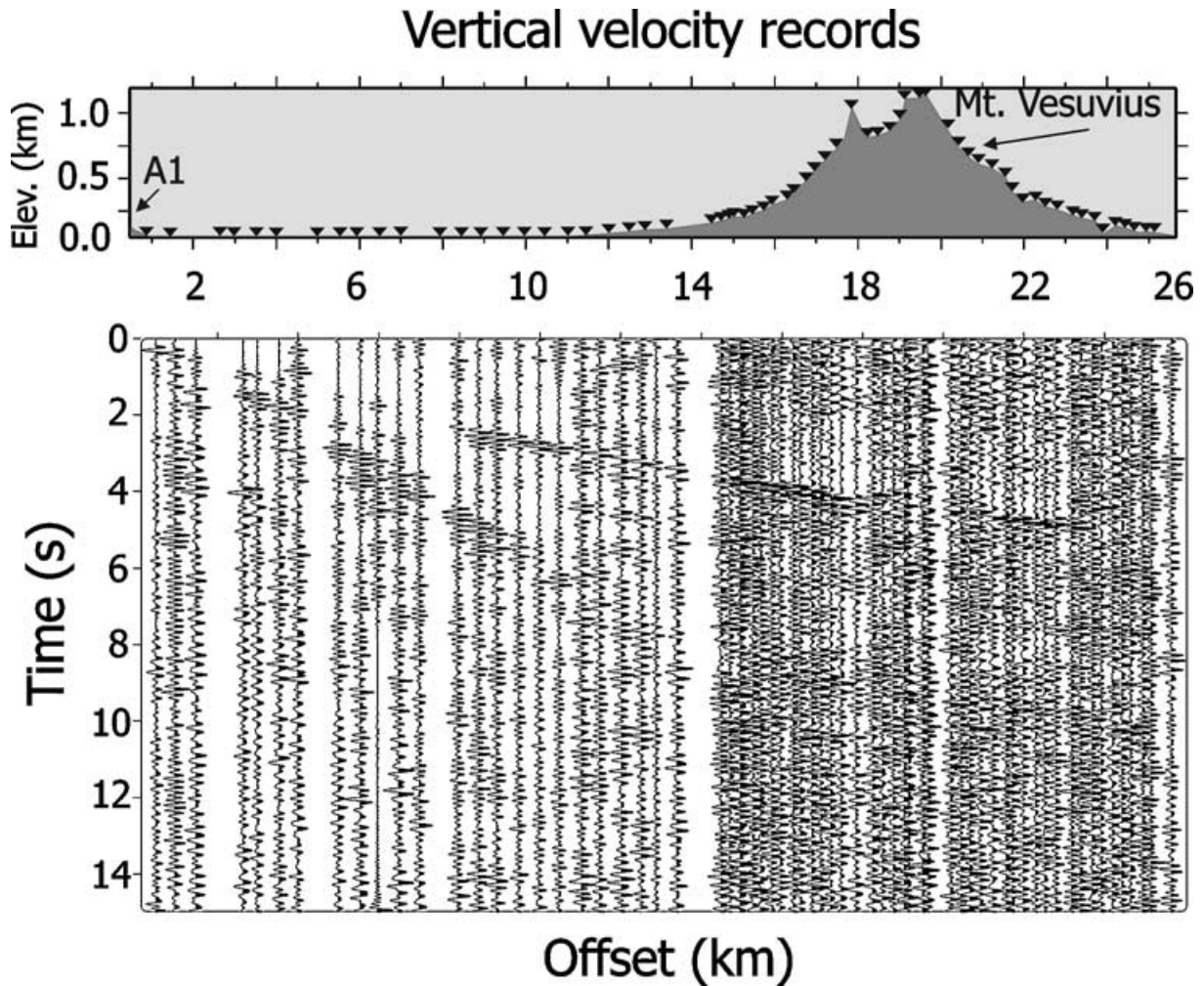


Figure 2. Examples of recorded seismic sections (see Fig. 1 for location). The records of the vertical ground motion velocity (amplitude is in arbitrary units) are displayed as a function of the offset (m) from the shot point. Traces have been bandpass filtered and AGC (variable width window) processed. (a) Along the profile A for the shot A1. Station elevations (km) along the profile are also plotted. (b) Along the profile D for the shot D2 (reduced velocity plot), (c) Along the profile C for the shot C3 (reduced velocity plot), (d) Along the profile B for the shot B2 (reduced velocity plot).

residual computation but only for limiting the number of models to explore, assigning a small probability to models predicting first arrival times larger than t_C . In Fig. 3 some examples of picking of times t_A , t_B and t_C are reported, while examples of traveltime curves for shots along profiles A and C are displayed in Fig. 4. Most travel-time curves show a significant change in the slope at offsets of 2–5 km from the shot points. This sharp transition of the traveltime curves is likely to be related to the arrival of a head-wave generated at the discontinuity between the volcanic/alluvial sediments and the Mesozoic limestone which is the prominent lithological transition at shallow depths (less than 3 km) underneath the Campanian plain and the volcanic complex.

4 BAYESIAN ESTIMATION OF MODEL PARAMETERS

4.1 Model parametrization and solution of the forward problem

The tomographic method we have applied is based on the search for the maximum likelihood solution in the model parameter space, i.e. the space of possible values for P -velocity at nodes of a 2-D grid.

The 2-D velocity field is parametrized by a regular grid of nodes which bring the model velocity parameters, as done by (Jin & Madariaga 1993). The velocity at any point of the medium is computed through a 2-D cubic spline interpolating function (Virieux 1991). We denote with $\mathbf{m} \equiv \{m_1, \dots, m_M\}$ the M -dimensional model parameter vector, whose components are the values of P -wave velocity at arbitrarily ordered grid nodes.

The ray tracing method is based on the numerical integration of the ray equation using the parameter τ defined as $ds = v^{-1} d\tau$ where ds is the elementary length along the ray path and v is the local velocity value (Cerveny 1987; Virieux *et al.* 1988). The following iterative formulae are obtained (Virieux *et al.* 1988; Zollo *et al.* 2000):

$$\begin{aligned} \mathbf{p}_{i+1} &= \alpha(\mathbf{r}_i)\tau + \mathbf{p}_i, \\ \mathbf{r}_{i+1} &= \frac{1}{2}\alpha(\mathbf{r}_i)\tau^2 + \mathbf{p}_i\tau + \mathbf{r}_i, \\ T_{i+1} &= T_i + v^{-2}\tau + \alpha(\mathbf{r}_i) \cdot \mathbf{p}\tau^2 + 1/3\alpha(\mathbf{r}_i)^2\tau^3, \end{aligned} \quad (1)$$

where \mathbf{p} is the ray parameter vector, \mathbf{r} is the ray position and T the traveltime at a given point in the propagation medium, given their initial values \mathbf{p}_0 , \mathbf{r}_0 and T_0 . The vector quantity α is the gradient of

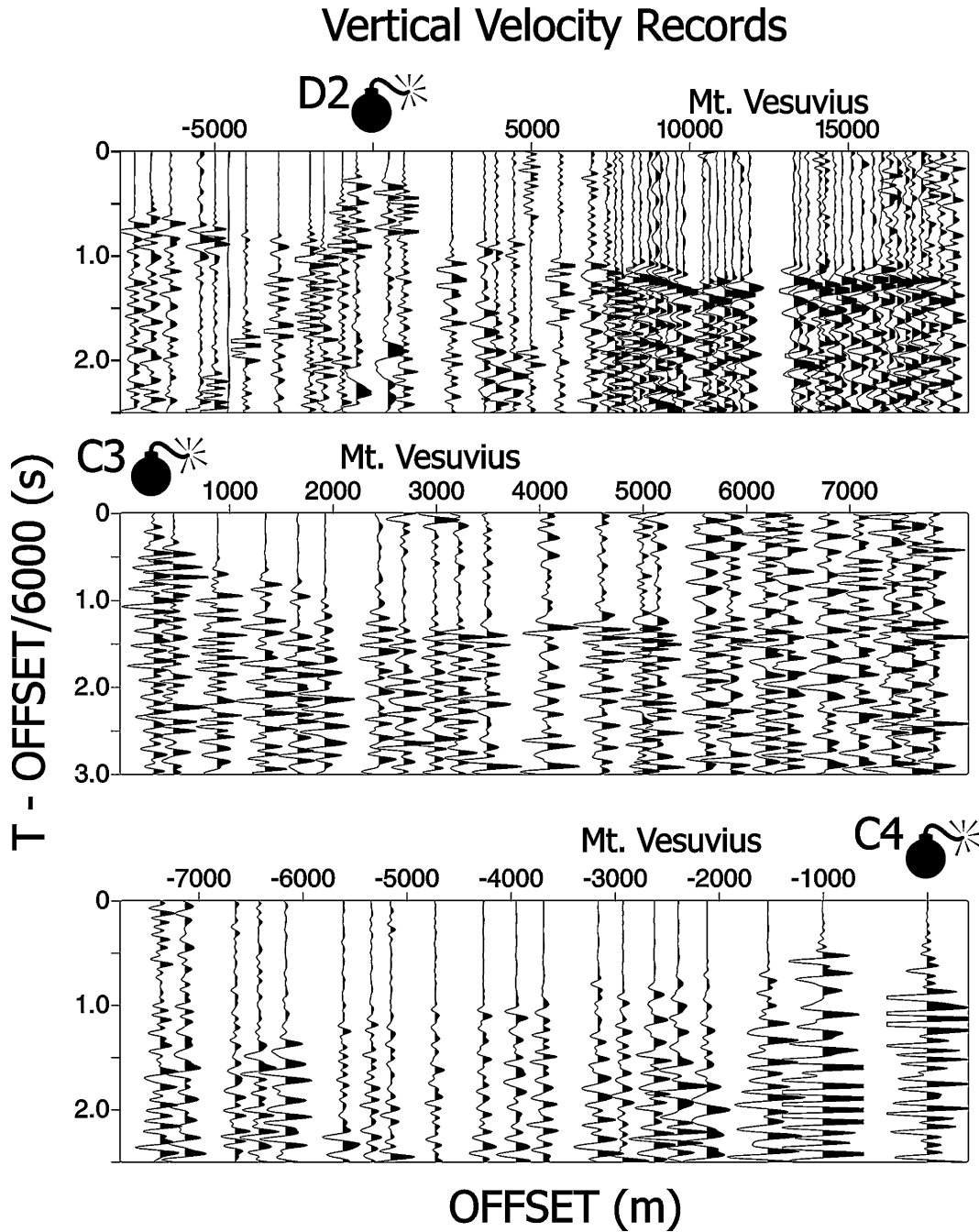


Figure 2. (Continued.)

squared slowness, which can be computed analytically for different 2-D interpolating functions (cubic spline, polynomial, Fourier series). The cubic spline interpolating function has been used here to compute the velocity values at any point of the 2-D gridded medium, providing a faster solution of the forward problem.

The ray tracing method used in this work is a classical two-point approach based on a shooting technique.

4.2 Posterior probability function by using the Bayes' rule

Let us consider the arrival time data set collected during an active seismic experiment consisting of $N = \sum_{i=1}^{N_S} N_i$ measurements of times t_A , where N_S is the number of sources and N_i is the number

of observed arrival times for the i th source. Assuming that for each individual data point the expected errors are Gaussian distributed with zero mean, we can define the conditional pdf of the observed first P -arrival times ($\mathbf{d} \equiv [d_1, \dots, d_N]$), given a model parameter vector \mathbf{m} :

$$p(\mathbf{d}|\mathbf{m}) = \text{const} e^{\left[\frac{-E(\mathbf{d},\mathbf{m})}{2\sigma_0^2} \right]}. \quad (2)$$

In eq. (2), E is the cost function of the optimization problem defined by:

$$E = \sum_{i=1}^{N_S} \sum_{j=1}^{N_i} w_{ij} (t_{ij}^{\text{obs}} - t_{ij}^{\text{cal}})^2, \quad (3)$$

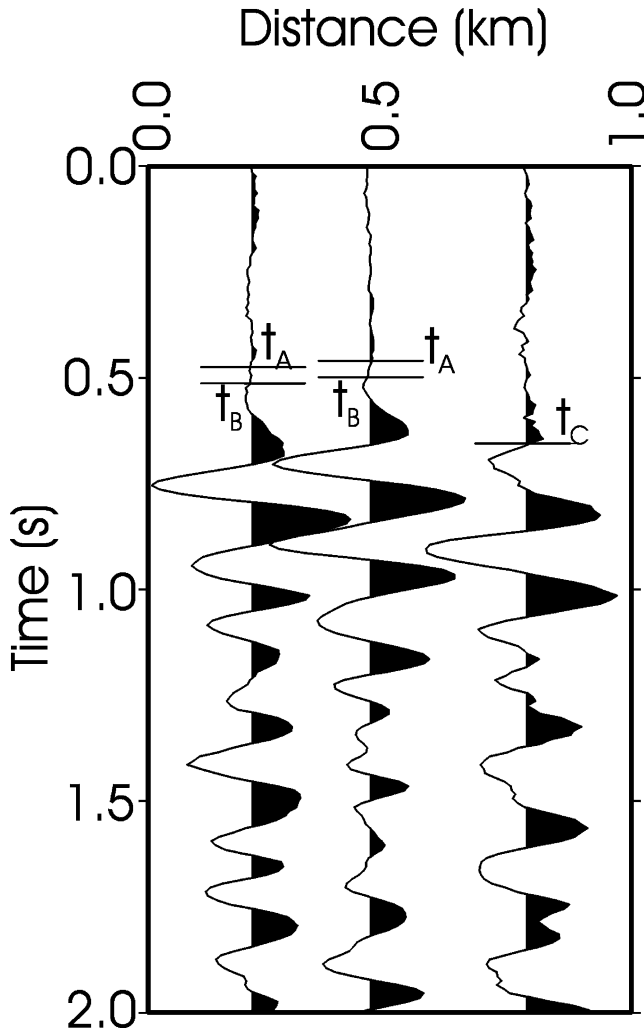


Figure 3. Example of picking of times t_A , t_B and t_C on recorded traces.

where t^{obs} and t^{cal} are the measured and computed first- P arrival times (t_A), and $w \propto |t_B - t_A|^{-1}$ is the normalized data weighting factor inversely related to the uncertainty on the time picking measurement. σ_o^2 is the unknown variance of arrival time data residual in eq. (3), which accounts for errors in modelling and in the data. This parameter determines the shape of the pdf eq. (2) and in our case has to be assigned arbitrarily, according to the expected best fit model variance.

In most geophysical problems, some *a priori* constraints on model parameters can be obtained and may be naturally considered in a Bayesian approach to the model parameter estimation problem. In our case, valuable constraints on the velocity model can be provided by (a) the minimum and maximum velocity compatible with rock lithology, geological and geophysical data in the investigated volume and by (b) the measurements of times t_C (see previous section) representing an upper limit for first P arrival time predicted by a given model. The use of the Bayes' rule gives a quantitative way to incorporate such *a priori* information on the model space and to compute the *a posteriori* probability $[p(\mathbf{m}|\mathbf{d}_o)]$ for \mathbf{m} , given an observed data vector \mathbf{d}_o :

$$p(\mathbf{m}|\mathbf{d}_o) = \text{const } p(\mathbf{d}_o|\mathbf{m}) \rho_1(\mathbf{m}) \rho_2(\mathbf{m}). \quad (4)$$

The constant in eq. (4) is the pdf normalization factor. Here, $\rho_1(\mathbf{m})$ and $\rho_2(\mathbf{m})$ are the prior probabilities of model parameters

which represent the state of knowledge about the model space before using the information provided by the data \mathbf{d}_o . In our case:

$$\rho_1(\mathbf{m}) = \prod_{k=1}^{N_C} \theta(t_{C_k}, t_k^{\text{cal}}(\mathbf{m})). \quad (5)$$

N_C is the number of t_C readings in the whole data set while the function θ is defined as

$$\theta(t_C, t^{\text{cal}}(\mathbf{m})) = \begin{cases} 1 & \text{for } t^{\text{cal}}(\mathbf{m}) < t_C \\ e^{\alpha(t_C - t^{\text{cal}}(\mathbf{m}))} & \text{for } t^{\text{cal}}(\mathbf{m}) > t_C \end{cases},$$

where α is an arbitrary positive constant.

The probability function $\rho_2(\mathbf{m}) = 1$ for $\mathbf{m} \in [\mathbf{m}_{\text{prev}} - \Delta\mathbf{m}, \mathbf{m}_{\text{prev}} + \Delta\mathbf{m}]$ and $\rho_2(\mathbf{m}) = 0$ elsewhere. \mathbf{m}_{prev} is a vector composed by the velocity values interpolated from a velocity model obtained in a previous iteration using a coarser medium discretization and $\Delta\mathbf{m}$ is an arbitrary assigned range. The definition of prior probability ρ_2 derives from the strategy of progressively densifying the number of grid nodes during the optimization process, which is detailed in the next paragraph. For the first optimization step $\rho_2(\mathbf{m}) = 1$ for $\mathbf{m} \in [\mathbf{m}_{\text{min}}, \mathbf{m}_{\text{max}}]$ where \mathbf{m}_{min} and \mathbf{m}_{max} are vectors whose components define the minimum and maximum allowable velocity value and $\rho_2(\mathbf{m}) = 0$ elsewhere.

4.3 The non linear optimization algorithm and strategy

The search for the model parameter vector maximizing the pdf eq. (4) is performed through a technique which uses, at consecutive steps, the Genetic Algorithm (GA) (Goldberg 1989; Whitley 1994) and the Simplex (SX) (Press *et al.* 1986) optimization methods. For practical purposes, the natural logarithm of pdf eq. (4) has been taken as the cost function, which has to be minimized. Both methods need only the cost function evaluation and not its derivatives. Among the different non-linear optimization methods (Monte Carlo, Simulated Annealing), the Genetic Algorithm has shown to be very efficient and fast for a wide exploration of a multi-parametric model space and for bracketing the region containing the absolute minimum (Boschetti *et al.* 1996; Sambridge & Drijkoningen 1992). Once the region of the model space which contains the absolute minimum of cost function is located by GA, the local minimum search is performed by SX which is in fact more efficient and fast for exploring cost functions having regular shapes, as one would expect nearby a local/absolute minimum.

We adopt an optimization strategy whereby several optimization runs are performed by progressively increasing the density of grid points describing the velocity field. At the very early stages (where the medium is parametrized by a very small number of parameters) the optimization is performed over a quite wide range of possible velocity values. Furthermore, for runs where the medium is discretized by a large number of grid nodes, the search is performed with smaller allowed velocity variations around a model interpolated from the one estimated in the previous run. These constraints on allowable velocities are set through the *a priori* probability $\rho_2(\mathbf{m})$ in eq. (4).

This non-linear search is embedded in a global strategy of model space sampling. As proposed by different authors, adaptive strategies of the model space sampling enables one to be independent of any initial estimation of the velocity field (i.e. Bijward *et al.* 1998).

The proposed strategy of model space reconstruction is equivalent in principle to move from a low to high wavenumber description of the velocity field which has been widely used in seismic tomography (Lutter *et al.* 1990) and in migration techniques where it is known

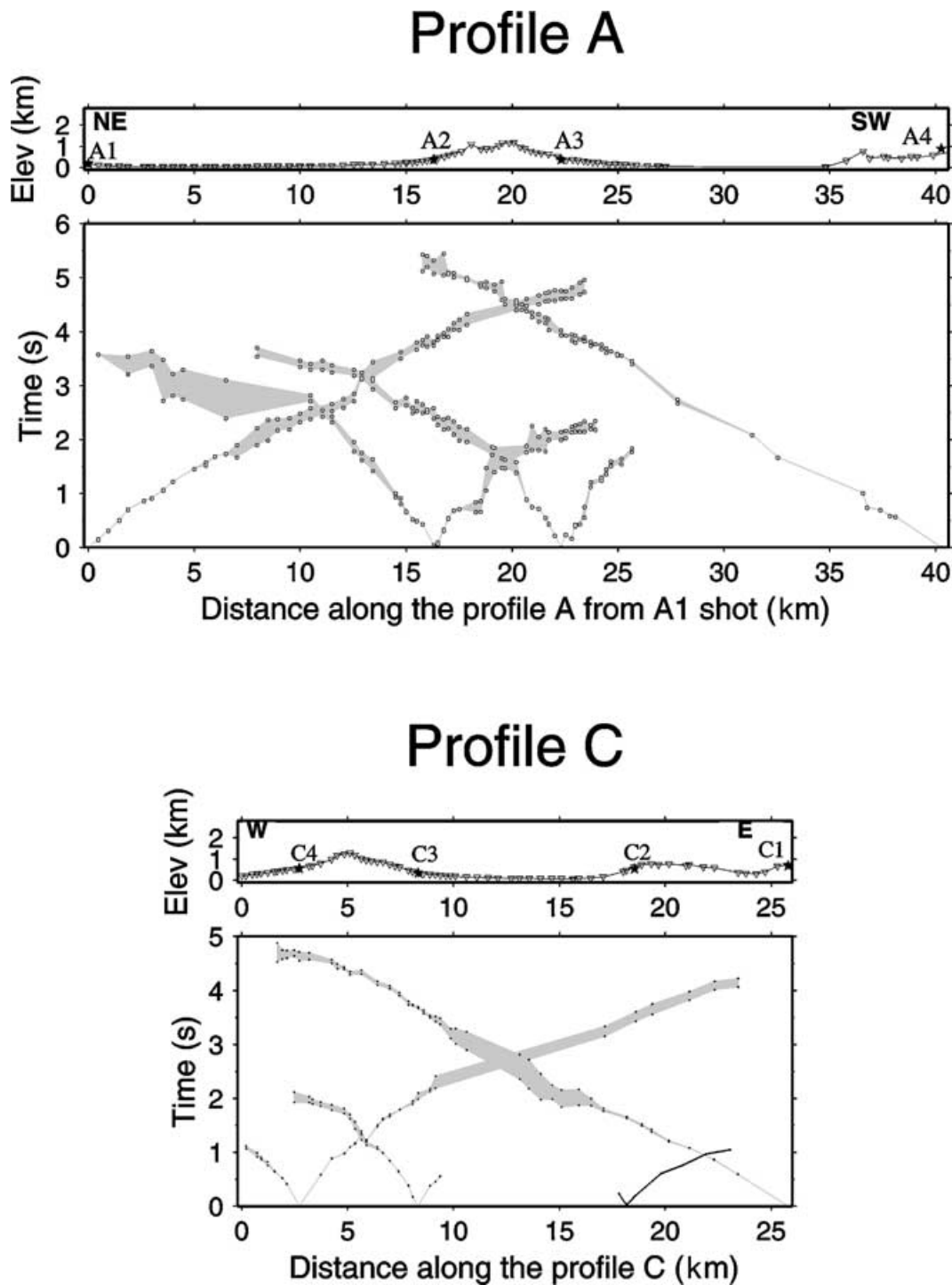


Figure 4. Examples of first P -arrival time curves for shots along profile A and C. The times t_A and t_B (see text for definition) are plotted at each receiver position along the profiles. Single time pickings indicate t_C .

as the ‘multi-scale’ approach (Bunks *et al.* 1995; Jin & Beydoun 2000).

The optimization procedure has been validated by synthetic tests assuming heterogeneous target models and sparse acquisition layouts (Zollo *et al.* 2000) (see next section). In particular the chosen strategy of progressively increasing the number of grid points makes the model parameter estimation robust and very efficient in terms of computing times.

4.4 Minimum of Akaike Information Criterion estimate

A point which needs to be considered concerns the evaluation of the statistical significance of models described by a different number of parameters. Moving from a low to high wavenumber description of the target medium, we ask for a criterion based on which we can decide whether to stop or continue the optimization process with a new, denser medium gridding. This point is addressed by the *Akaike*

Information Criteria (AIC) which was first introduced by Akaike (1974) for model selection and subsequently applied to earthquake statistics and seismic source problems (e.g. De Natale *et al.* 1988; Yoshida 1989). Among the best-fit models described by a different number of parameters, one is selected which minimizes the function:

$$\text{AIC} = -2 \max(\text{likelihood}) + 2(\text{number of parameters}) \quad (6)$$

where likelihood is the *a posteriori* pdf in eq. (2). To search for a minimum AIC corresponds to finding the best compromise between the goodness of fit and the model simplicity (small number of parameters). By introducing the minimum AIC criterion, the problem of selecting the optimal medium parametrization is formulated without the need for subjective decision required in the classical approaches based on hypothesis-testing or variance comparison. When two models described by a different number of parameters provide the same likelihood value, the one defined by the smaller number of parameters is chosen. In other words, the minimum AIC criterion gives a mathematical formulation of the principle of parsimony in model building.

In literature, other related statistical analyses can be found as the Extended Information Criterion (EIC) that has been used for assessing the objective determination of damping parameters in tomographic problems (Aoike *et al.* 1998).

5 *P*-VELOCITY MODELS OF MT VESUVIUS REGION

The final 2-D *P*-velocity models for the Mt Vesuvius and surrounding area have been obtained using the optimization technique and strategy described above. They correspond to vertical sections along the profiles A, B, C, D and S reported in Fig. 1. The profile of the 1994 active seismic campaign (labelled S in Fig. 1) has been reprocessed in this work although a velocity model was already obtained for this line but it used both active and local earthquake data and a different tomographic technique (Zollo *et al.* 1998).

The length of the investigated section is fixed *a priori* for each profile, based on the specific geometry of the acquisition lay-out. The maximum section depth is fixed at 5 km b.s.l. based on results about 1-D *P*-velocity models in the area obtained in a previous work (De Matteis *et al.* 2000).

For each analyzed profile, the optimization procedure is started from an initial model parametrized by a 4×2 rectangular grid. At successive runs the number of grid points is generally doubled both in the horizontal and vertical direction, thus progressively increasing the spatial model sampling. For a given number of grid nodes, the search for the maximum likelihood model is performed using both the Genetic (GA) and Simplex (SX) algorithms and stopped when the derivative of cost function vs the iteration number approaches zero within an arbitrary fixed threshold. An example of the convergence history for a given model parametrization is displayed in Fig. 5.

We always set for the GA a crossover probability of 0.8 and a mutation probability of 0.05. The population size is chosen depending on the number of model parameters. We found that a good compromise between GA efficiency and computation time is a population whose size is about 3–5 times the number of parameters.

A decrease of the final model variance moving from models with small to large number of parameters is generally observed. In order to assess the statistical significance of this fit improvement, the parameter AIC is computed and the model for which the AIC value is minimum is chosen as the best fit model. The AIC has been

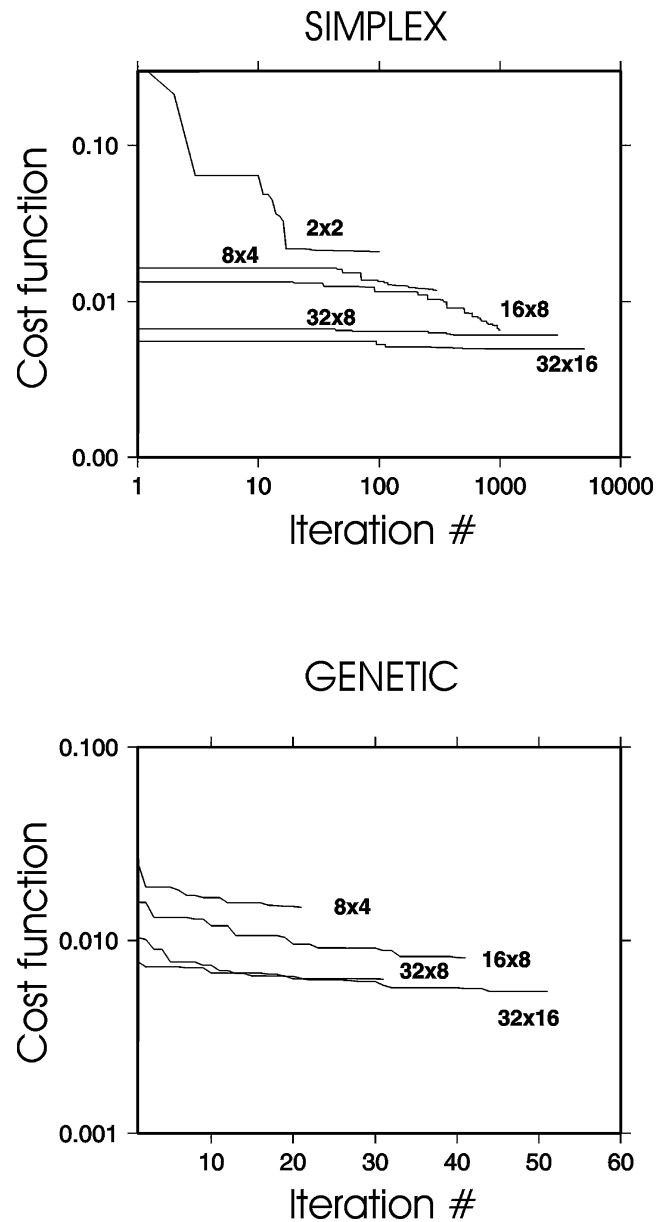


Figure 5. Example of the convergence history of the optimization process. The Figure shows the decreasing pattern of the function $\log(\text{Probability})$ vs the iteration number for each parametrization (number of grid nodes). (Top) convergence history for the Simplex optimization run. (Bottom) convergence history for the Genetic Algorithm optimization run.

computed for the different analyzed profiles and for different combination of the number of grid points along the *x* and *z* directions of the model. Table 1 resumes the results of this analysis.

All the investigated profiles present a minimum AIC (values in rectangles) for models described by 16×8 nodes, with the exception of profile D where the minimum AIC is found for the 8×4 geometry. The minimum resolvable wavelength is variable along the vertical and horizontal directions. The minimum cell size is also variable from one profile to another due to the different profile length. The average value of the minimum horizontal cell dimension resolved by data varies between 1.7 km (profile B) to 3.8 km (profile D) while the vertical one ranges from 0.9–1 km (profiles A, B, C and S) to 2 km (profile D). Due to the dominant horizontal *P*-wave propagation, the vertical resolution is higher, as expected.

Table 1. Estimate of AIC for different model parametrizations. N_x and N_z are the number of nodes along the x - and z -directions, respectively. The reported minimum AIC values are shown in bold.

$N_x \times N_z$	A	B	C	D	S
4×2	7136	6574	3635	2508	1977
8×4	1482	602	1201	349	831
16×8	1283	569	719	431	684
32×16	1402	1123	1318	1124	1348
RMS of the minimum AIC model (sec^2)	0.007	0.005	0.005	0.004	0.006

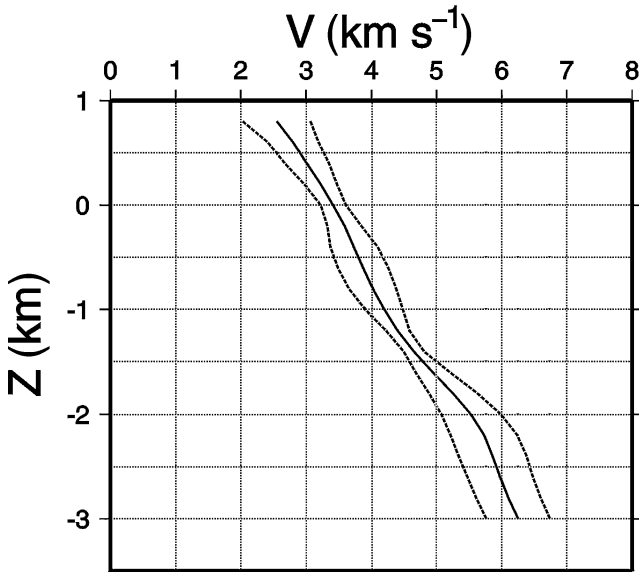


Figure 6. Average 1-D velocity model underneath Mt Vesuvius. The Figure shows the 1-D average model (with 1σ confidence limits) extracted from different 2-D model sections in a radius of 1.5 km from the crater axis.

With the aim to investigate the vertical variation P -velocity beneath the Mt Vesuvius cone, we extracted a representative number of 1-D curves along the retrieved 2-D section in a radius of 1 km from the cone down to about 3 km depth. In Fig. 6 the mean P -velocity value and the $\pm 1\sigma$ error bounds are reported as a function of depth from the volcano topography. The error limits account for both the lateral medium heterogeneity inside the selected earth cylinder and for the uncertainties on the velocity estimations along the different 2-D sections. The average model shows a nearly linear increase (2.5 to 4.5 km s^{-1}) of P -velocity with depth from the volcano top down to 1.5 km depth and a smooth transition to higher velocities (5.5 to 6.0 km s^{-1}) at larger depths.

The 2-D tomographic images relative to the five analyzed profiles are shown in Fig. 7. From the top to the bottom the displayed sections correspond to moving clockwise from the North to the South. All the model sections are oriented from the Appennines outcrops to the volcano and are aligned in order to have the Mt Vesuvius cone at the same location. For completeness, the profile A is also represented at the figure bottom but in the reversed direction.

Overall, the inferred images show a high variability of P -velocities in the shallow structure, with values ranging from 1.5 km s^{-1} to 6 km s^{-1} . A very sharp velocity increase (from 3–4 km s^{-1} to 6 km s^{-1}) is observed at depths ranging from a few hundreds meters to 3–4 km. These values and their variation with depth are consistent with the laboratory measurements of ultrasonic (1 MHz source fre-

quency) P and S velocities in dry and water saturated rock samples recovered from the Trecase well, recently performed by Bernard & Zamora (2000).

The checkerboard analysis (see next section) of the retrieved images shows that the best resolved areas are located beneath the volcanic complex where the maximum ray coverage and intersection is expected for the planned acquisition lay-out. The dashed lines in model sections displayed in Fig. 7 delimitate at depth the areas where model anomalies are best resolved as inferred from the checkerboard analysis.

6 ERROR AND RESOLUTION ANALYSIS

The probability function in eq. (4) contains the complete information about the problem of model parameter estimation and its shape in the M -dimensional space directly provides a global image on the uncertainty and resolution of parameters in the model space.

Due to the high non-linearity of the tomographic problem, this information is difficult to retrieve using numerical methods. We propose different approaches for the error and resolution estimation. The errors on model parameters are obtained by the local exploration of the probability function eq. (4) around the maximum likelihood model. The model resolution is studied by the ‘checkerboard test’ analysis (see next paragraph) which accounts for the non-linearity of the tomographic inverse problem. In addition, a number of simulated inversions are performed to investigate the capability of the method to retrieve specific geometric features which appear in the best fit model. The latter helps into understand how the model parametrization influences the shape and intensity of the retrieved anomalies.

6.1 Error estimation

Jackson & Matsu’ura (1985) propose to obtain valuable estimates of uncertainties on model parameters from the analysis of the marginal pdf, i.e. the probability for a single parameter m_i obtained by integrating the ‘posterior’ pdf over the volume defined by parameters $m_j \neq m_i$. Tarantola & Mosegaard (1995) and Sen & Stoffa (1996) proposed different methods for the computation of marginal pdf based on the *importance sampling* algorithms. Due to the high number of parameters, the computation of the marginal pdfs is not feasible in our case. In fact, the adequate sampling of the model parameter space for evaluating the probability integral would require too large a number of forward model computations.

For this reason, we used an approximate method to estimate the uncertainty on velocity at grid nodes based on the computation of cross-section of the *posterior* pdf in eq. (4):

$$p_C(m_i) = \frac{p(\mathbf{m}|m_j = m_j^{\text{best}})}{\int p(\mathbf{m}|m_j = m_j^{\text{best}}) dm_i} \quad \text{with } j \neq i, \quad (7)$$

where $p_C(m_i)$ is the pdf for parameter i , given the parameters $j \neq i$ fixed at the maximum likelihood values (\mathbf{m}^{best}). For a given maximum likelihood model parameter vector, the cross-section pdf of parameter m_i is computed by varying it in a given range and fixing the other parameters at the values they take in the maximum likelihood model. Examples of cross-section plots of pdf for velocity parameters varying along the model section are shown in Fig. 8. The error on parameter m_i is therefore estimated as the 1σ interval measured on the cross-section pdf plots. In this way the estimate of the parameter uncertainty is done locally at the maximum likelihood

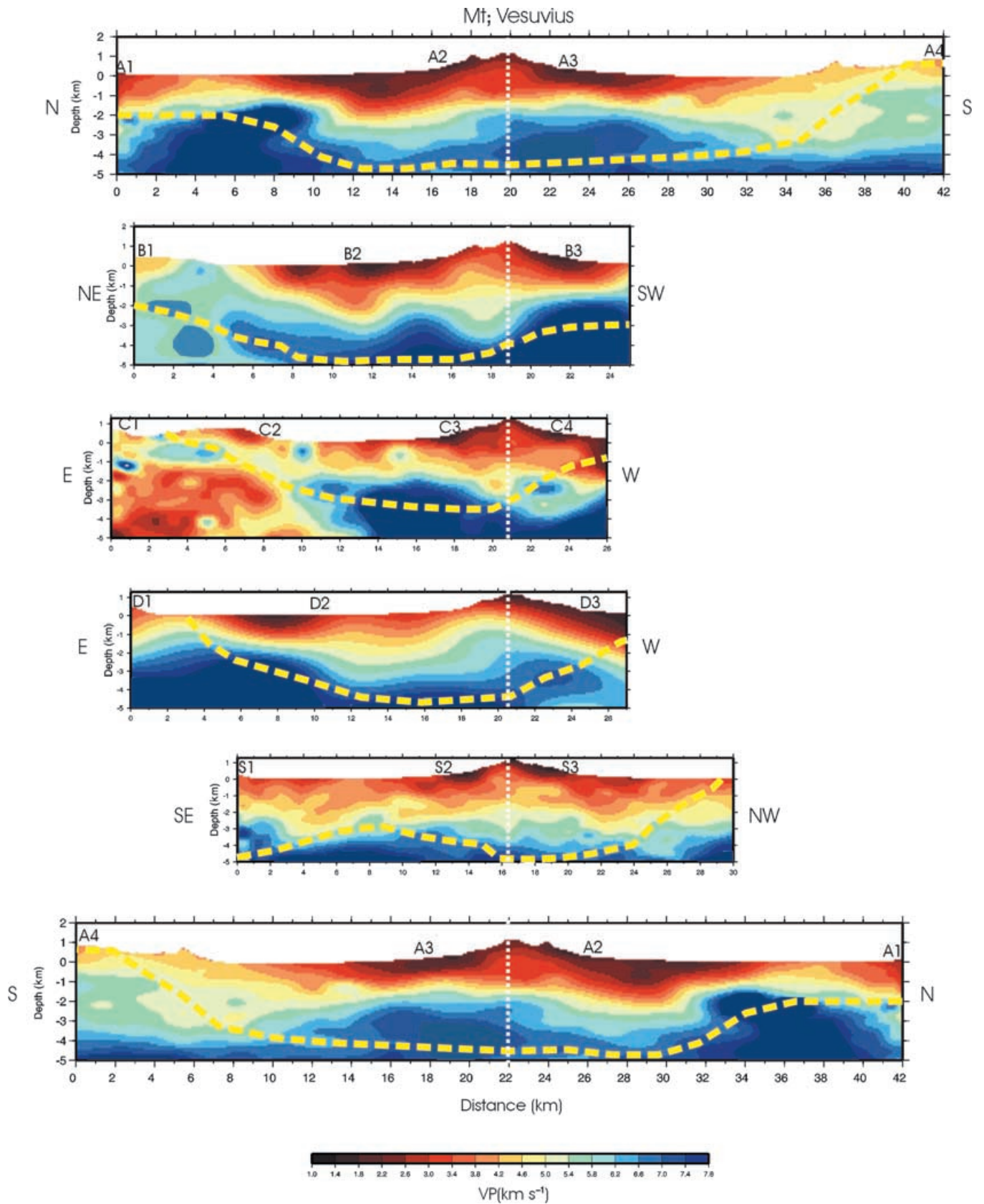


Figure 7. Results of the present tomographic study. 2-D *P*-velocity models for the Campanian Plain and Mt Somma–Vesuvius volcanic complex. Top to the bottom the Figure shows the model sections relative to profiles A (from A1 to A4), B, C, D, S and again A (from A4 to A1). According to the radial geometry of the active seismic experiments, the 2-D models have been arranged with the Mt Vesuvius cone at the same horizontal position and clockwise from N to S. The dashed line delineates at depth the best resolved areas as qualitatively inferred from the checkerboard resolution tests (Fig. 9).

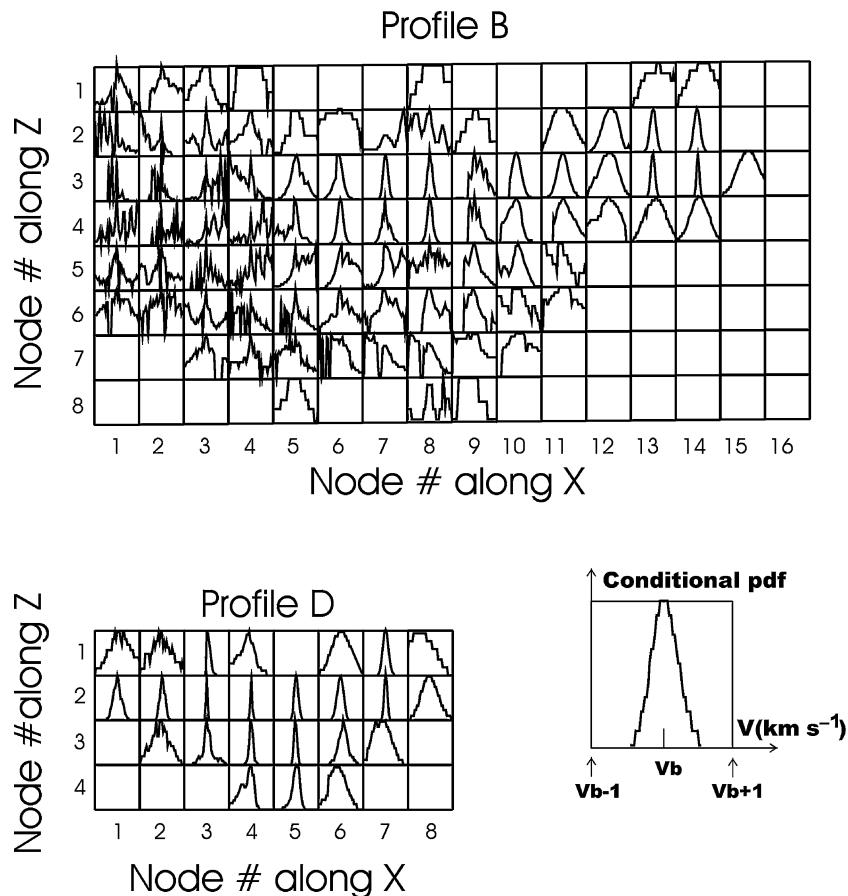


Figure 8. Example of cross-section plots of the *a posteriori* pdf computed on real data for the maximum likelihood model relative to the profiles B and D. For each node the pdf is plotted in a square box, normalized to its maximum value. The velocity axis is centred at the best fit value (V_b) and extends from $V_b - 1$ km s⁻¹ to $V_b + 1$ km s⁻¹. Accurate parameter estimates correspond to curves with a narrow gaussian-like shape. Poorly resolved parameters show curves which appear highly irregular and multi-modal. White boxes indicate a nearly flat pdf in the explored velocity range.

point by disregarding any possible correlation with the other parameters and assuming that no other relevant maxima of the pdf exist. This is somewhat similar to the estimate of the covariance matrix in linear or linearized tomographic approaches but considering only its diagonal elements, i.e. the parameter variances (Menke 1984).

6.2 Checkerboard tests

The checkerboard tests are commonly used for assessing the model reliability and to define the spatial resolution of tomographic images and to investigate the spatial parameter correlation (Zelt 1998). The 2-D medium is subdivided in cells as for the maximum likelihood discretized model. The checkerboard model is obtained by adding a small positive and negative quantity (± 10 m s⁻¹ in our case) to the velocity values of each grid node, alternatively. The amount of perturbation is chosen in order that the ray paths in the checkerboard model match closely the ones traced in the best-fit model. Higher perturbations dramatically change the ray paths geometries with respect to the ones in the final model, make unstable the non-linear inversion process and give a false resolution estimation. The optimization procedure is therefore applied to synthetic first arrival times computed for the checkerboard model. The spatial variation of parameter resolution is displayed by the residual image obtained by subtracting point by point the retrieved and *true* checkerboard models. Highly resolved regions are the ones where the shape and

amplitude of the anomalies reproduce well the original checkerboard pattern. In Fig. 9 are shown the 1σ error maps and the results of the checkerboard test for each of the analyzed profiles. Generally, poorly resolved areas show relatively large errors on velocity and an undefined checkerboard pattern. However the error and checkerboard maps may not correlate, the latter being more sensitive to the degree of spatial parameter correlation. Errors on velocity parameters are smaller at shallow depths ($< 2-3$ km b.s.l.) and underneath the volcano complex ($0.3-0.8$ km s⁻¹) and increase at greater depths and moving outside the volcano edifice. Fig. 10 displays the pattern of rays and the arrival time residuals $T^{\text{obs}} - T^{\text{cal}}$ vs distance for the profile A, computed for the best fit (minimum AIC) model. The residuals are mostly confined in the range ± 0.07 s (which represents the 1σ interval) although a larger scatter is observed for large offset data. A similar pattern is observed for all the other profiles.

6.3 Fixed-geometry tests

Furthermore, we performed a number of simulated inversions ('fixed geometry' tests). The term 'fixed geometry' is used here for *P*-velocity anomalies having a given shape and spatial extension. The fixed geometry tests provide information about the capability of the method and data to retrieve the main geometrical features appearing in the best fit model (e.g. extension, shape and amplitude

Profile A

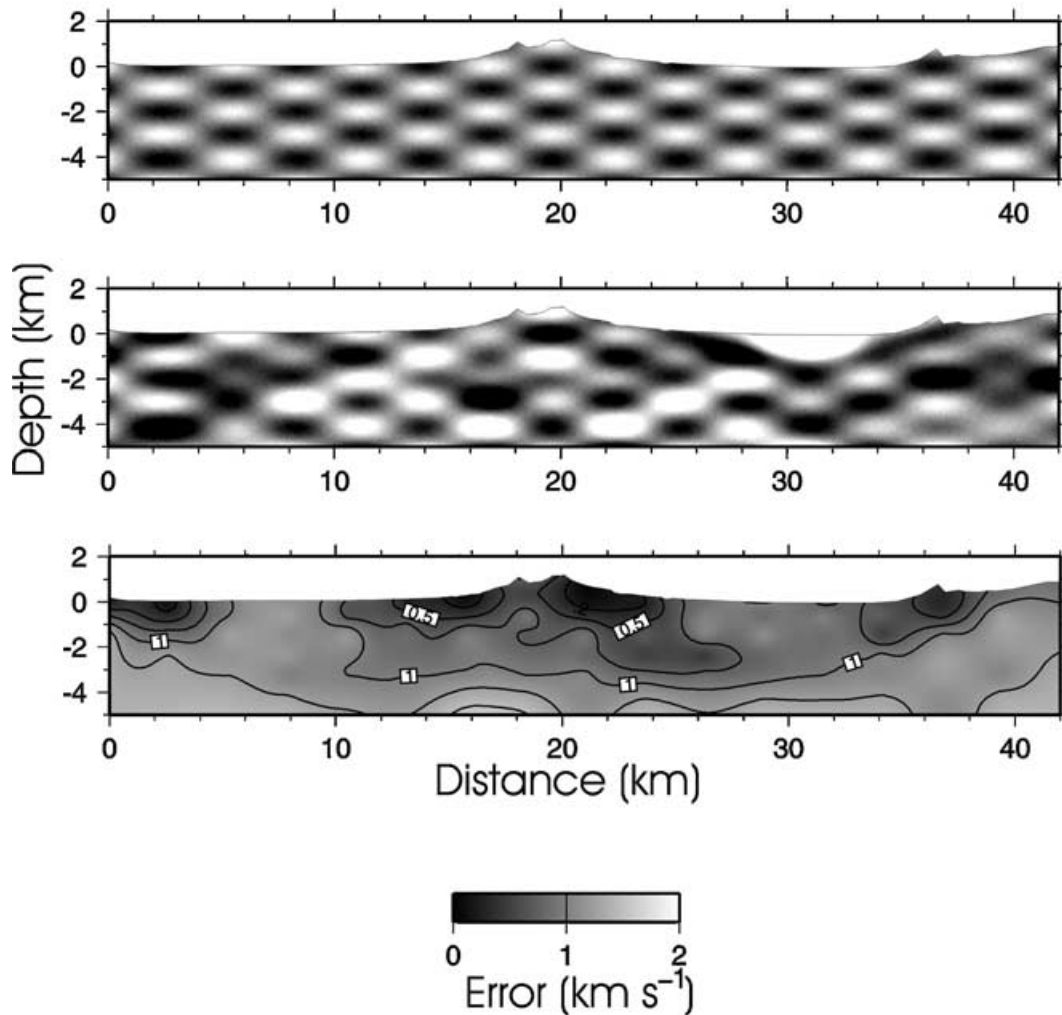


Figure 9. The results of the checkerboard test and error maps for the maximum likelihood models obtained for all the analyzed profiles. For each profile are shown the reference checker-board model (Top), the estimated checker-board model (Middle) and the 1σ error map computed from the cross-section probability plots. The color scale unit in error maps is in km s^{-1} . (a) Profile A; (b) Profile A; (c) Profile C; (d) Profile D; (e) Profile S.

of velocity anomalies, layer dipping and undulation). It consists in the generation and inversion of a series of synthetic arrival times computed for a given velocity model which contains the geometric features to be checked. Synthetic data are computed for the acquisition lay-out which reproduces the real data acquisition. In our case the test aims at assessing the significance and reliability of the morphology of the 2000–3000 m deep sharp P -velocity transition and the high V_p body beneath the summit caldera retrieved from the modelling of the true data set.

The fixed geometry model is depicted in Fig. 11 along with models obtained by using different numbers of grid points. The retrieved models are arranged in order of increasing grid point numbers from the top to the bottom. Synthetic P -arrival times have been computed for the configuration of sources and receivers of the Mt Vesuvius experiments. In particular the test reproduces the acquisition lay-out of profile A (Fig. 1). We note that the shape and extension of the

shallow sedimentary layer is well recovered even in low wavenumber models. Due to the medium description by a continuous velocity field, the interface between the sedimentary and carbonatic layer is modelled as a transition zone, (the velocity interval between 4 and 5 km s^{-1} iso-velocity curves, in Fig. 6) which become sharper as we move from low to high wavenumber models. The iso-velocity contour at $4.5\text{--}5 \text{ km s}^{-1}$ seems to better fit the location and shape of the interface in the reference model ('true' in figure). As an effect of the cubic-spline interpolation, the poor resolved zones in the deeper part of the sections show artificial velocity undulations and overestimated values. On the other hand, the method is able to (a) retrieve with sufficient accuracy the extension and thickness of the depression in the interface (between 9 and 17 km), (b) to detect the high velocity area located just above the interface (between 17 and 22 km) and (c) to determine the absolute velocity field in the shallow sedimentary layer underneath the volcanic edifice.

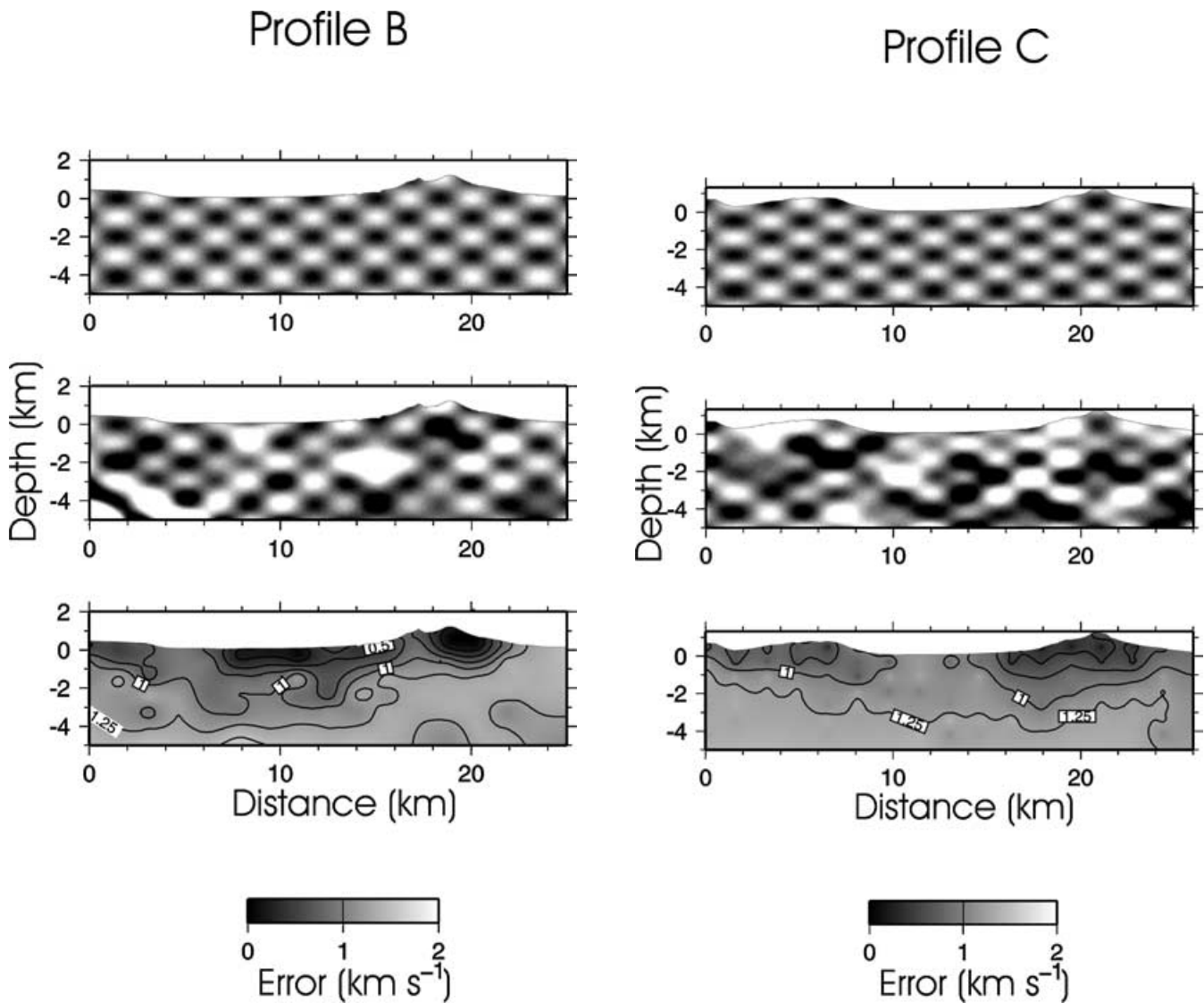


Figure 9. (Continued.)

7 DISCUSSION AND CONCLUSIONS

In this paper we applied a Bayesian approach for modelling first- P arrival times collected during two active seismic experiments at Mt Vesuvius. The inversion method is based on the massive computation of the *a posteriori* probability density function which relates observed and predicted data. Its maximum in the multi-dimensional parameter space is searched by applying at successive steps, global (Genetic) and local (Simplex) optimization techniques. The 2-D propagation medium is described by a cubic spline interpolating function and traveltimes are computed by using the ray theory. The mean computation time for a typical Mt Vesuvius section (40 km \times 5 km) is about 50 hr on a Linux based PC, with Pentium II 400 MHz processor. This is the time required for the whole inversion process, including the search for the model parametrization by using the multi-scale approach. We believe that the use of more powerful computers may permit the extension of the methodology on larger data set and to 3-D acquisition layouts.

The adopted approach allows us to naturally include physical constraints on the velocity model in the form of an *a priori* probability density function. Constraints are here represented by the assigned

bounds on P -velocity values and by times t_C picked on noisy, far-offset records, representing an upper limit for first P arrival time predicted by a given model.

The gridding of the target medium is a critical choice in seismic tomography. The minimum medium wavelength resolved by first arrival time data is generally unknown *a priori* depending critically on the spatial velocity distribution. The applied optimization strategy is based on the progressive increase of the number of grid nodes to describe the velocity anomalies. At each step the model obtained in the previous run is re-sampled with a larger number of grid points and the new search is started, allowing for velocity variations within a given, arbitrary wide range. Early steps of the optimization process (when the medium is described by a small number of grid points) are performed without any *a priori* starting model, allowing for the whole exploration of the velocity space. This approach is equivalent to move from a low to high frequency description of the medium anomalies. Synthetic applications showed that it is more stable and robust with respect to consider from the beginning a very dense model gridding.

For the inversion of Mt Vesuvius arrival time data, we generally adopted the strategy of doubling the number of parameters both in

Profile D

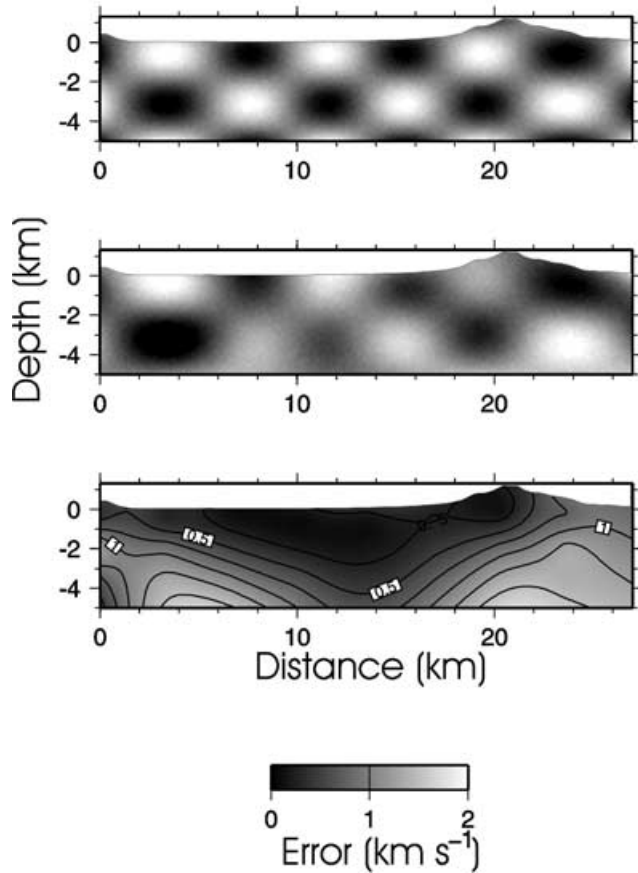


Figure 9. (Continued.)

the horizontal and in the vertical direction (starting from a 4×2 initial model) which implies a model description by equal size cells. This is the most natural choice, in absence of any *a priori* information on the model resolution. The optimal medium parametrization (maximum number of grid nodes) is chosen according to the Akaike Information Criterion, which expresses the principle of parsimony, i.e. the selected model is the one that represents the best compromise between the goodness of fit and the model simplicity (small number of parameters). The application of AIC to Mt Vesuvius' tomographic models shows that the minimum horizontal cell dimension resolved by data varies between 1.7 km and 3.8 km while the vertical one is smaller, ranging from 0.9–1 km to 2 km. We point out that this corresponds to an average resolved wavelength along the investigated depth sections, but the checkerboard tests performed on the models retrieved using different grid sizes show that resolution is strongly variable spatially over the depth sections.

The 2-D images of Mt Vesuvius and Campanian Plain show a sharp P -velocity increase at a depth range of 2000–3000 m. Lithostratigraphic analyses (Principe *et al.* 1987) and laboratory ultrasonic measurements on rock samples (Bernard & Zamora 2000) from the Trecase well indicate that it corresponds to the top of the Mesozoic limestone formation. It can be reasonably assumed that the P -velocity isoline at 5000 m s^{-1} marks the position of this discontinuity in our tomographic images.

The limestone top appears to have an irregular shape and generally dips from the edges of the Campanian Plain toward the volcano. This trend is also consistent with the Bouguer anomaly pattern shown in Fig. 1 (Cassano & La Torre 1987; Berrino *et al.* 1998).

The head waves generated at the limestone top are continuously recorded at receivers installed on the whole volcano edifice (Fig. 2). This indicates that the morphology of the limestone top is rather continuous also underneath the volcano. Considering that the recorded seismic waves have wavelengths of about 200–400 m at 8 Hz and the station spacing is 250 m, only the irregularities larger than about 300 m can be resolved.

The shape of the limestone top as inferred by the present study (isoline at 5.0 km s^{-1}) is also consistent with information from other shallow seismic data (Bruno *et al.* 1998) acquired by AGIP

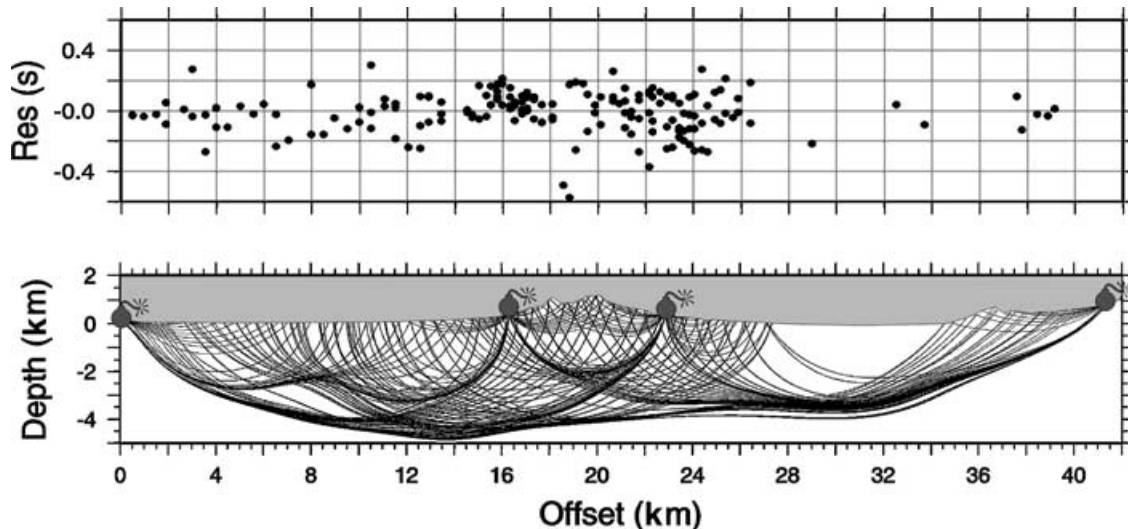


Figure 10. (Top) Plot of first P arrival time (t_A) residuals vs distance along the same profile. (Bottom) Ray-tracing in the maximum likelihood model for profile A.

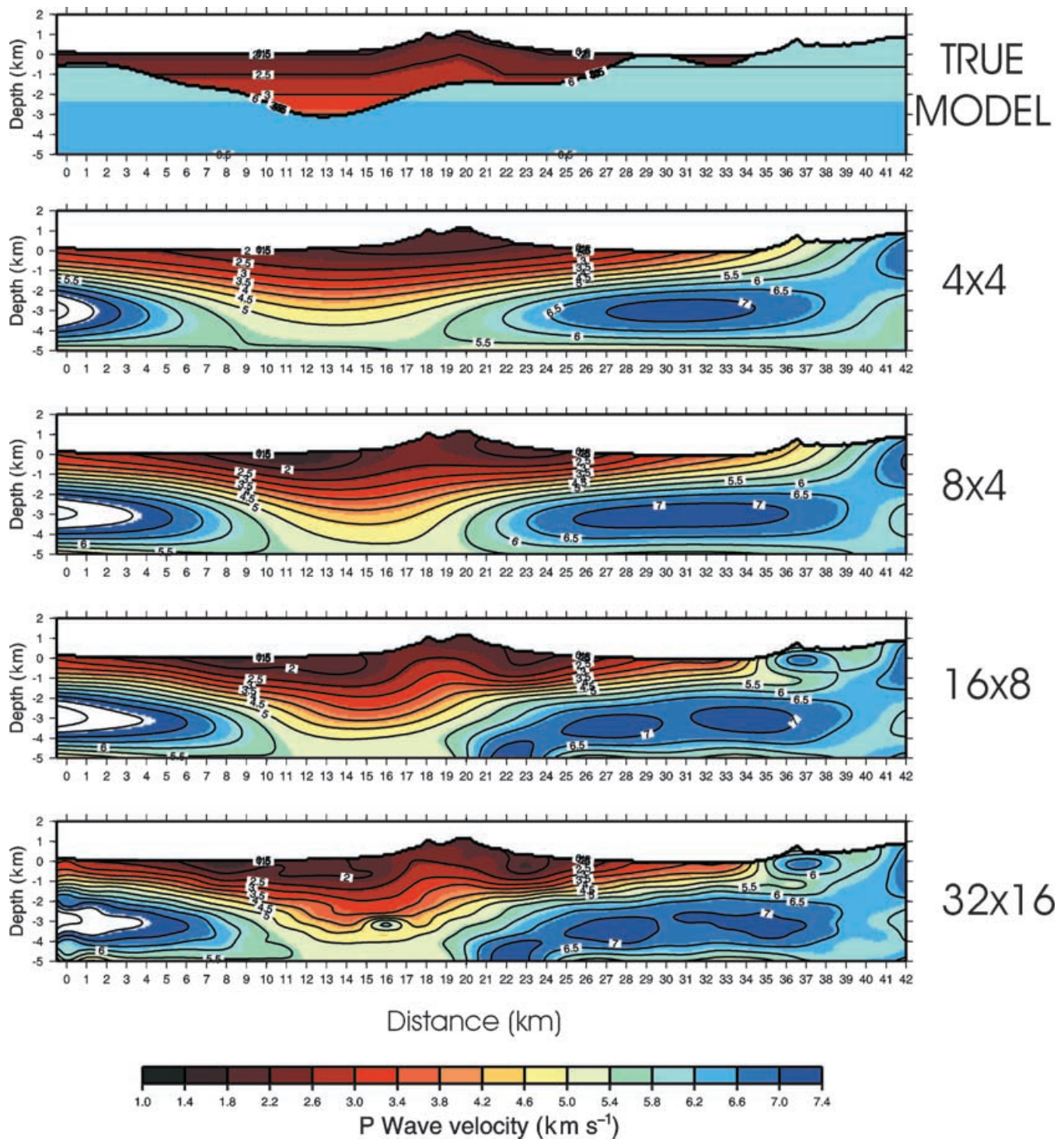


Figure 11. Fixed-geometry resolution test. On the top the 2-layer reference model used for synthetic simulations is shown. It reproduces characteristic features of the inferred Mt Vesuvius models. In particular, it contains the irregular shaped interface simulating the Mesozoic limestone top which dips toward the volcano, the depression of this reflector NE of Mt Vesuvius and the high velocity body underneath the volcano edifice. Maximum likelihood models are shown for an increased grid density (the number of nodes are reported right of each model section).

(Italian Petroleum Agency) in the plain surrounding the volcano edifice.

Looking in detail at the tomographic model for profile A, the prominent feature is the presence of an approximately 1 km deep and 8 km wide depression of the limestone top located below the N edge of the volcano. Its southern limit is just underneath the Mount

Somma caldera. This depression is well resolved by the used optimization method as displayed by the *ad hoc* fixed geometry synthetic test (Fig. 6). North of the depression all the seismic data indicate a gradual northward uplift of limestone top while at the South the depth of the limestone top from seismic data is consistent with that observed in the stratigraphic log of the Trecase well located near the

shot A3 (Fig. 1). Analyses of fluvial deposits in the Campanian Plain indicate that in this area a thickening of low density sediments is expected for the barrier effect produced by the Mt Somma–Vesuvius edifice (Di Vito *et al.* 1999).

In the layer overlying Mesozoic limestones, P velocities change from near surface values of 1.5–1.7 km s⁻¹ to 3.5–4.5 km s⁻¹ at depth. A prominent feature of the tomographic images is a relatively high velocity region ($v_p = 3.5$ –4.5 km s⁻¹) located 1–1.5 km underneath the summit caldera of the volcano visible in all the profiles. The high velocity body overlaying the Mesozoic limestones underneath the summit caldera can be associated with a palaeo-volcanic or a sub-volcanic (solidified dikes) structure. In fact the range of observed velocities is consistent with *in situ* and laboratory measurements of solidified lavas (Bernard 1999; Zamora *et al.* 1994). As suggested by De Natale *et al.* (2000) it can represent a volume of quenched magma, produced by a sudden increase of the solidus temperature after extensive degassing consequent to strong explosive activity.

REFERENCES

- Akaike, H., 1974. A new look at the statistical model identification, *IEEE Trans. Autom. Contr.*, **6**, 716–723.
- Aoike, K., Nishizawa, O. & Sato, T., 1998. Application of the extended information criterion to seismic tomography using local earthquakes, *Proc. SEGI Int. Symp.*, **55**, 153–160.
- Aster, R. & Meyer, R.P., 1988. Three-dimensional velocity structure and hypocenter distribution in the Campi Flegrei caldera, Italy, *Tectonophysics*, **149**, 195–218.
- Benz, H.M. & Smith, R.B., 1984. Simultaneous inversion for lateral velocity variations and hypocenters in the yellowstone region using earthquake and refraction data, *J. geophys. Res.*, **89**, 1208–1220.
- Bernard, M.-L., 1999. Etude expérimentale des propriétés physique des roches pyroclastiques de la Montagne Pelee, *PhD thesis*, Université de Paris VII, France.
- Bernard, M.-L. & Zamora, M., 2000. Mechanical properties of volcanic rocks and their relations to transport properties, *EOS, Trans. Am. geophys. Un.*, **81**, Fall Meet. Suppl., Abstract V71A-33.
- Berrino, G., Corrado, G. & Riccardi, U., 1998. Sea gravity data in the Gulf of Naples: a contribution to delineating the structural pattern of the Vesuvian area, *J. geophys. Res.*, **82**, 139–150.
- Bijward, H., Spakman, W. & Engdahl, E.R., 1998. Closing the gap between regional and global travel time tomography, *J. geophys. Res.*, **103**, 30 055–30 078.
- Boschetti, F., Dentith, M.C. & List, R.D., 1996. Inversion of seismic refraction data using genetic algorithms, *Geophysics*, **61**, 1715–1727.
- Bruno, P.G., Cippitelli, G. & Rapolla, A., 1998. Seismic study of the mesozoic carbonate basement around Mt. Somma–Vesuvius, Italy, *J. geophys. Res.*, **84**, 311–322.
- Bunks, C., Saleck, F.M., Zaleski, S. & Chavent, G., 1995. Multi-scale seismic waveform inversion, *Geophysics*, **60**, 1457–1473.
- Cassano, E. & La Torre, P., 1987. Geophysics, in *Somma–Vesuvius*, pp. 175–196, ed. Santacroce, R., CNR Editions, Rome.
- Cerveny, V., 1987. *Ray Tracing Algorithms in Three Dimensional Laterally Varying Layered Structures in 'Tomography in Seismology and Exploration Seismics'*, Nolet and Reidel, Hingham, MA.
- De Luca, G., Filippi, L., Patane, G., Scarpa, R. & Vinciguerra, S., 1997. Three-dimensional velocity structure and seismicity of Mt. Etna volcano, Italy, *J. Volc. Geotherm. Res.*, **79**, 123–138.
- De Matteis, R., Zollo, A. & Virieux, J., 1997. P-wave arrival time inversion by using the $\tau - p$ method: application to Mt Vesuvius volcano, *Geophys. Res. Lett.*, **24**, 515–518.
- De Matteis, R., Latorre, D., Zollo, A. & Virieux, J., 2000. 1-D P-velocity models of Mt Vesuvius Volcano from the Inversion of TomoVes96 First Arrival Time Data, *Pageoph*, **157**, 1643–1661.
- De Natale, G., Musmeci, F. & Zollo, A., 1988. A linear intensity model to investigate the causal relation between Calabrian and north-Aegean earthquake sequence, *Geophys. J. Int.*, **95**, 285–293.
- De Natale, G., Petrazzuoli, S.M., Troise, C., Pingue, F. & Capuano, P., 2000. Internal stress field at Mount Vesuvius: A model for background seismicity at a central volcano, *J. geophys. Res.*, **105**, 16 207–16 214.
- Di Vito, M.A., Sulpizio, R., Zanchetta, G. & Calderoni, G., 1999. The geology of the south western slope of Somma–Vesuvius, Italy, as inferred by borehole stratigraphies and cores, *Acta Vulcanologica*, **10**, 383–393.
- Evans, J.R. & Zucca, J.J., 1988. Active high resolution seismic tomography of compressional wave velocity and attenuation at Medicine Lake Volcano, Northern California Cascade Range, *J. geophys. Res.*, **93**, 15 016–15 036.
- Finetti, I. & Morelli, C., 1974. Esplorazione sismica a riflessione dei Golfi di Napoli e Pozzuoli, *Boll. Geofis. Teor. Appl.*, **16**, 122–175.
- Gallart, J., Driad, L., Charvis, P., Sapin, M., Hirn, A., Diaz, J., de Voogd, B. & Sachpazi, M., 1999. Perturbation to the lithosphere along the hotspot track of La Réunion from an offshore-onshore seismic transect, *J. geophys. Res.*, **104**, 2895–2908.
- Gasparini, P. & TomoVes Working Group, 1998. Tomoves: A project of seismic investigation of Mt Vesuvius, *EOS, Trans. Am. geophys. Un.*, **79**, 229–231.
- Goldberg, X., 1989. *Genetic Algorithm in Search, Optimization and Machine Learning*, Addison-Wesley Pub Co., Boston.
- Hammer, P.T.C., Dorman, L.M., Hildebrand, J.A. & Cornuelle, M.D., 1994. Jasper seamount structure: seafloor seismic refraction tomography, *J. geophys. Res.*, **99**, 6731–6752.
- Ippolito, F., Ortolani, F. & Russo, M., 1973. Struttura marginale tirrenica dell'appennino campano: Reinterpretazione di dati di antiche ricerche di idrocarburi, *Mem. Soc. Geol. It.*, **XII**, 227–250.
- Jackson, D.D. & Matsu'ura, M., 1985. A bayesian approach to nonlinear inversion, *J. geophys. Res.*, **90**, 581–591.
- Jin, S. & Madariaga, R., 1993. Background velocity inversion with a genetic algorithm, *Geophys. Res. Lett.*, **20**, 93–96.
- Jin, S. & Beydoun, W., 2000. 2-D multiscale non-linear velocity inversion, *Geophys. Prospect.*, **48**, 163–180.
- Lees, J.M. & Crosson, R.S., 1989. Tomographic inversion for three dimensional velocity structure at Mount St Helens using earthquake data, *J. geophys. Res.*, **94**, 5716–5728.
- Lutter, W.J. & Nowack, R.L., 1990. Inversion of crustal structure using reflections from the PASSCAL Ouachita experiment, *J. geophys. Res.*, **95**, 4633–4646.
- Menke, W., 1984. *Geophysical Data Analysis: Discrete Inverse Theory*, International Series, Academic Press, San Diego CA.
- Mosegaard, K. & Tarantola, A., 1995. Monte Carlo sampling of solutions to inverse problems, *J. geophys. Res.*, **100**, 12 431–12 448.
- Nercessian, A., Hirn, A. & Tarantola, A., 1984. Three dimensional seismic transmission prospecting of the Mont Dore volcano, France, *Geophys. J. R. astr. Soc.*, **76**, 307–315.
- Press, W.H., Flannery, B.P., Teukolsky, S.A. & Vetterling, W.T., 1986. *Numerical Recipes*, Cambridge University Press, Cambridge.
- Principe, C., Rosi, M., Santacroce, R. & Sbrana, A., 1987. Geophysics, in *Somma–Vesuvius*, pp. 11–52, ed. Santacroce, R., CNR Editions, Rome.
- Sambridge, M. & Drijkoningen, G., 1992. Genetic algorithms in seismic waveform inversion, *Geophys. J. Int.*, **109**, 323–342.
- Scandone, R., Bellucci, F., Lirer, L. & Rolandi, G., 1991. The structure of the Campanian Plain and the activity of the Neapolitan volcanoes Italy, *J. Volc. Geotherm. Res.*, **48**, 1–31.
- Sen, M.K. & Stoffa, P.L., 1996. Bayesian inference, Gibbs' sampler and uncertainty estimation in geophysical inversion, *Geophys. Prospect.*, **44**, 313–350.
- Thurber, C.H., 1984. Seismic detection of the summit magma complex of Kilauea volcano, Hawaii, *Science*, **223**, 165–167.
- Virieux, J., 1991. Fast and accurate ray tracing by Hamiltonian perturbation, *J. geophys. Res.*, **96**, 579–594.
- Virieux, J., Farra, V. & Madariaga, R., 1988. Ray tracing in laterally heterogeneous media for earthquake location, *J. geophys. Res.*, **93**, 6585–6599.

- Whitley, D., 1994. A Genetic Algorithm Tutorial, Samizdat Press (http://samizdat.mines.edu/ga_tutorial).
- Yoshida, S., 1989. Waveform inversion using ABIC for the rupture process of the 1983 Hindu Kush earthquake, *Phys. Earth planet. Int.*, **56**, 389–405.
- Zamora, M., Sartoris, G. & Chelini, W., 1994. Laboratory measurements of ultrasonic wave velocities in rocks from the Campi Flegrei volcanic system and their relation to other field data, *J. geophys. Res.*, **99**, 13 553–13 561.
- Zelt, C.A., 1998. Lateral velocity resolution from 3-d seismic refraction data, *Geophys. J. Int.*, **135**, 1101–1112.
- Zhao, D., Hasegawa, A. & Horiuchi, S., 1992. Tomographic imaging of P and S wave velocity structure beneath NE Japan, *J. geophys. Res.*, **97**, 19 909–19 928.
- Zhu, X., Sixsta, D.P. & Angstman, B.G., 1992. Tomo-statics: Turning-ray tomography + static corrections, *The Leading Edge*, **11**, 15–23.
- Zhu, X., Angstman, B.G. & Sixta, D.P., 1998. Case history. overthrust imaging with tomo-datuming: a case study, *Geophysics*, **63**, 25–38.
- Zollo, P. *et al.*, 1998. An image of Mt Vesuvius obtained by 2-D seismic tomography, *J. Volc. Geotherm. Res.*, **82**, 161–173.
- Zollo, A., De Matteis, R., D'Auria, L. & Virieux, J., 2000. A 2-D non linear method for travelttime tomography: Application to Mt Vesuvius active seismic data, in *Problems in Geophysics for the Next Millenium*, pp. 125–140, eds Boschi, E., Ekstrom, G. & Morelli, A., ING-Editrice Compositori, Bologna.